# Effect of annealing temperature on the structural, morphological, photocatalytic and optical properties of the Cu-Ni co-doped $TiO_2$ nanoparticles

M. S. Basir, S. N. Supardan, S. A. Kamil*
[a]*Faculty of Applied Sciences, Universiti Teknologi MARA, 40450, Shah Alam, Selangor, Malaysia*

The effect of annealing temperature on the photocatalyst's structural, morphological, photocatalytic and optical properties have been extensively studied. In this work, the Cu-Ni co-doped $TiO_2$ powder was prepared by the sol-gel technique and annealed at temperatures 400°C, 500°C, 600°C, 700°C, and 800°C. The structural phase of the Cu-Ni/$TiO_2$ changed from anatase to rutile after the annealing temperature increased from 400°C to 800°C. The anatase phase was found at 400°C and 500°C, the mixed phase at 600 and 700°C, and the rutile phase at 800°C. The specific surface area and band gap of Cu-Ni/$TiO_2$ were decreased with the increment of annealing temperatures from 70.00 to 24.89 $m^2/g$ and 3.36 eV to 3.04 eV, respectively. Meanwhile, as the annealing temperature rises, the average particle size increases from 38.52 to 173.59 nm. The anatase-rutile mixed phase of Cu-Ni/$TiO_2$ annealed at 600°C exhibited the highest photocatalytic degradation of methylene blue (MB) with 62.81% MB removal. Experimental results indicated that the annealing temperature could alter the structural, morphological, and optical properties of the Cu-Ni/$TiO_2$, affecting the photocatalytic activity performance.
(Received; Accepted)

(Received March 8, 2023; Accepted July 17, 2023)

*Keywords:* Cu-Ni/$TiO_2$ nanoparticles, Annealing temperature, Mixed-phase, Sol-gel, Photocatalytic degradation

## 1. Introduction

Titanium dioxide ($TiO_2$) is an n-type semiconductor which is the most suitable photocatalyst in the photocatalysis process because $TiO_2$ has fascinating properties such as low toxicity, good thermal and chemical stability, low cost, and high photoactivity efficiency [1]–[3]. Due to these advantages, $TiO_2$ is widely used for various applications such as for photocatalysis water treatment [4], gas sensors [5], solar cells [6], and air purification [7]. Generally, $TiO_2$ exists in three major structural phases, which are anatase, rutile, and brookite [1]–[3]. Anatase and rutile are the most common structure phases reported from previous studies, in which rutile is stable at high temperatures while anatase is at low temperatures. D.K Muthee et al. reported that the anatase phase was formed at an annealing temperature of 450°C with a small brookite peak, while the rutile phase was formed at a high temperature above 650°C [8]. M.K. Sight et al. reported that the rutile transformation occurred at 800°C [9]. Besides that, R. Dubey also reported that $TiO_2$ annealed at 450°C exhibits an anatase phase and at 700°C exhibits a rutile phase [10]. Meanwhile, brookite is an unstable phase and not suitable for photocatalytic activity [11].

As compared to the rutile phase, the anatase phase has slower charge carrier recombination [10], good electron mobility [12], a small grain size, and higher surface areas [13]. Meanwhile, the rutile phase has a rapid rate of electron-hole ($e^-$ and $h^+$) recombination, large particle size and surface area [14], [15]. Nevertheless, despite these advantages, anatase has a wide band gap of 3.2 eV, which makes it unsuitable under visible light sources for the photocatalytic process. However, some previous researchers reported that the anatase-rutile mixed phase is an alternative structural phase for photocatalytic activity. This phase can increase the photocatalytic performance under visible light instead of UV light [16]. According to F. Weiwei et al., the mixed phase exhibits a higher

* Corresponding author: suraya_ak@uitm.edu.my
https://doi.org/10.15251/DJNB.2023.183.841

photodegradation efficiency under visible light because the anatase-rutile mixed phase can shift the absorption band to the visible light region and this mixed phase can increase the surface area of the $TiO_2$ photocatalyst [17]. G. K. Min et al. reported that the anatase-rutile mixed phase with anatase as a dominant phase composition resulted in the best photoactivity performance with a rate constant of $3.11\times10^{-2}$ $min^{-1}$ due to the mixed phase providing the lower electron-hole pairs recombination rate compared to the single anatase and rutile phase [18].

Currently, most $TiO_2$ photocatalyst studies are directed towards enhancing the photocatalytic activity by reducing the recombination rate of the electron-hole pair of the $TiO_2$ [11]. The metal ions such as Cu [19], Ni [20], Ag [21], and Fe [22] have been utilized widely for doping with $TiO_2$ to reduce the band gap and recombination of photoinduced holes- electrons pair of the $TiO_2$ which resulting an excellent efficiency of photoactivity [11]. According to Wang M. et al., the existence of copper ion ($Cu^{2+}$) effectively could prevent the recombination of $e^-$ and $h^+$ sites, and increase the photocatalytic activity [19]. L. S. Yoong et al. reported that hydrogen production of Cu doped is much higher than pure $TiO_2$, indicating high photocatalytic activity [23]. Other metal, such as nickel (Ni), also exhibits great photocatalytic performance, as reported by Liu Y. et al., which Ni/$TiO_2$ attributed to the great photo-generated electron-hole pair efficiency [20]. The same results were reported by Jing D. et al., the presence of nickel ion ($Ni^{2+}$) served as trapping sites on the surface of the $TiO_2$ and reduced the surface recombination of electron-hole pairs [24]. Moreover, a co-doping technique has been reported in previous studies which has a higher photocatalytic activity than single doping of $TiO_2$ [25], [26]. It has been reported by Behnajady M. A. et al., the rate constant for degradation of acid orange 7 (AO7) dye for Ag-Cu/$TiO_2$ is 0.0953 $min^{-1}$ was higher than single doped Cu/$TiO_2$, which is 0.0745 $min^{-1}$ [27]. Shaban M. et al. reported the co-doping of Ni-Cr/$TiO_2$ applied for the degradation methylene blue resulting in the degradation percentage for co-dopant Ni-Cr/$TiO_2$ is 95.6%, higher than single doped Ni/$TiO_2$ [28].

During the phase transition from anatase to rutile phase, the crystallite size, lattice parameters, stoichiometry of the nanostructure, crystallite size, specific area, and pore structure also varied. The pore structure of the photocatalyst, such as mesopore, exhibits a higher specific surface area. These advantages promise more active sites to absorb organic pollutants such as azo dye, and the diffusion of contaminant molecules is more accessible inside the pores of the $TiO_2$ [29], [30]. Based on the abovementioned factors, studying the role of annealing temperature is essential because the annealing temperature can affect the $TiO_2$ structural, morphological, and optical properties, which eventually affecting the photocatalytic activity.

## 2. Experimental

### 2.1. Materials

Titanium (IV) butoxide, $C_{16}H_{36}O_4Ti$ (Sigma Aldrich >97% purity) was used as titanium dioxide precursor. Copper (II) nitrate trihydrate, $Cu(NO_3)_2\cdot3H_2O$ (Analytical Reagent) (R&M >99% purity) and nickel nitrate hexahydrate, $Ni(NO_3)_2\cdot6H_2O$ (Analytical Reagent) (Chemiz >99% purity) were used as a dopant metal while ethanol, $C_2H_6O$ (HmbG >99% purity) as a solvent. Methylene blue (Bendosen, $C_{16}H_{18}CIN_3S$) was used as a model dye in this study.

### 2.2. Synthesis of Cu and Ni co-doped $TiO_2$ Nanoparticles (Cu-Ni/$TiO_2$)

Cu-Ni/$TiO_2$ nanoparticles were prepared by the sol-gel technique. 55 ml of ethanol and 26 ml of titanium (IV) butoxide were stirred for 1 hour, and the mixture was labelled as solution A. After that, 55 ml of ethanol and 5 ml of deionized water were mixed and labelled as solution B. Later, solution B was added into solution A to slow down the hydrolysis process, and the mixture of solution A and B became solution C. After that, solution C was stirred for 4 hours. Then, 3 wt% of copper and nickel metal salt with a ratio of 9:1 (copper: nickel) was added into solution C. Solution C was left to be stirred overnight without any heating process to ensure the solution mixed properly. Then, solution C underwent the ageing process for 48 hours, and the titanic gel was obtained. Later, it was dried at 120°C for 2 hours to ensure no unwanted ethanol remained in the solution. After that, Cu-Ni/$TiO_2$ powder was formed. The dried powder underwent pulverizing process using a ball mill pulverizer machine for 3 hours after the drying process was completed to

obtain a fine powder. Finally, the powder was annealed at a rate of 5°C/min at different temperatures for 3 hours. The samples were designated as CN-T4, CN-T5, CN-T6, CN-T7, and CN-T8 according to the annealing temperature of 400°C, 500°C, 600°C, 700°C, and 800°C, respectively.

### 2.3. Characterization of samples

In this study, Cu-Ni/$TiO_2$ nanoparticles were characterized using Thermal Gravimetric Analysis (TGA) (Perkin Elmer Pyris 1), Fourier-Transform Infrared Spectroscopy (FTIR) (Perkin Elmer FTIR Spectrum One), X-ray Powder Diffraction (XRD) (PANalytical X'pert PRO), Field Emission Scanning Electron Microscopy (FESEM) and Energy Dispersive X-ray (EDX) (Thermoscientific Apreo 2S FESEM and Bruker XFlash 6I100 EDX), and UV–Vis Diffuse Reflectance Spectroscopy (DRS) (Shimadzu). TGA was carried out to identify the suitable annealing temperature of Cu-Ni/$TiO_2$ nanoparticles. The samples were heated at a rate of 10°C/min from 27 to 900°C. Infrared absorption spectrum obtained from FTIR was used to identify the chemical bond in the samples. The phase compositions of the synthesized Cu-Ni/$TiO_2$ nanoparticles were identified by using XRD with Cu Kα (λ = 1.54060 Å) radiation of 45 kV and an accelerating voltage current of 40 mA. The 2θ scanning range was 5° to 90°, and the step size was 0.01°. Debye-Scherer's equation was used to calculate crystallite size of the samples. FESEM and EDX were employed to study the surface morphologies and elemental compositions, respectively. DRS recorded the reflectance spectrums at 200 to 2500 nm wavelength. The band gap of the Cu-Ni/$TiO_2$ nanoparticles were determined by using Kubelka–Munk function, F(R), and the extrapolation of Tauc plot.

### 2.4. Photocatalytic degradation test of Cu-Ni/$TiO_2$ nanoparticles

The photocatalytic performance of the Cu-Ni/$TiO_2$ was evaluated by degradation of methylene blue (MB). Cu-Ni/$TiO_2$ powder was added into aqueous 10 ppm MB solution, and the suspension was continuously stirred for 30 min dark condition to achieve the adsorption-desorption equilibrium during the reaction of photocatalyst and dye. The suspension was irradiated under UV light (Analytikjena, UVP UVGL-58, 6W, 254 nm) at room temperature for 2 hours. During the photodegradation process, the solution was withdrawn via a syringe every 10 min, and the MB concentration was evaluated using VIS spectrophotometer Genesys 30 single beam. The photocatalytic degradation performance (%) was calculated by using Eq. (1) [18]

$$Degradation\ percentage\ (D\%) = \left(\frac{C_0 - C_t}{C_0}\right) \times 100\% \quad (1)$$

where $\boldsymbol{C_0}$ is the initial absorbance and $\boldsymbol{C_t}$ is the absorption at a certain irradiation time $\boldsymbol{t}$ of the MB solution (λ = 664 nm).

## 3. Results and discussion

Fig. 1 shows the thermal gravimetric analysis (TGA) curve of Cu-Ni/$TiO_2$ nanoparticles. According to the TGA curve, the weight loss with a total mass of 28.47% of the Cu-Ni/$TiO_2$ from 27 to 900°C with a heating rate of 10°C/min heated in an air atmosphere occurs in two stages of weight loss. The first stage of weight loss at temperatures 30 to 280°C attributed to the decomposition of absorbed water and ethanol from the sample during the sol-gel process [9], [23], [31]. Meanwhile, the second stage of weight loss occurs from 530 to 900°C attributed to the decomposition of organic residues such as nitrate ($NO_3^-$) group from metal salt copper and nickel nitrate [23], [31]. Based on Fig. 1, the annealing temperature for Cu-Ni/$TiO_2$ at 400°C, 500°C, 600°C, 700°C, and 800°C with a duration of 3 hours was selected.

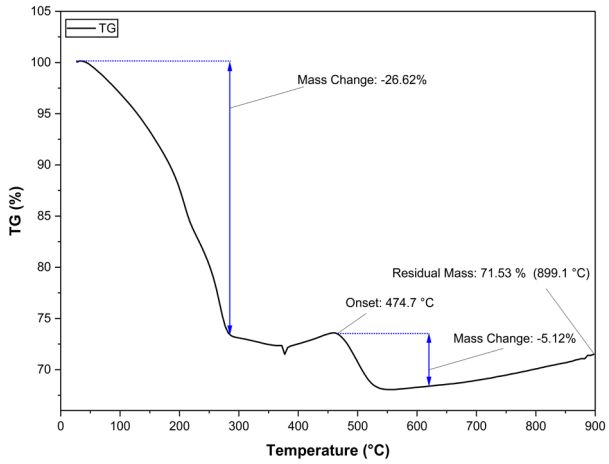


*Fig. 1. TGA curve of Cu-Ni/$TiO_2$ nanoparticles.*

Fig. 2 shows the FTIR spectrum of Cu-Ni/$TiO_2$ nanoparticles. The absorption peaks around 1630 $cm^{-1}$ and 3400 $cm^{-1}$ are attributed to the O-H bending and stretching, respectively [2], [23]. The stretching vibrations of Ti-O were found in the IR band between 500 and 900 $cm^{-1}$ [23], [32]. Based on the red dash line in Fig. 2, the increasing annealing temperature of Cu-Ni/$TiO_2$ causes a shift of Ti-O stretching vibrations at the range 500 and 900 $cm^{-1}$ towards lower energy due to the phase transition which from anatase phase to rutile phase [33]. The absorption band at 1366 $cm^{-1}$ was attributed to the presence of the nitrate ($NO_3^-$) group at low temperatures. However, the intensity of the $NO_3^-$ group decomposes as the absorption band was not observed when the annealed temperature was at 700°C and above [34].

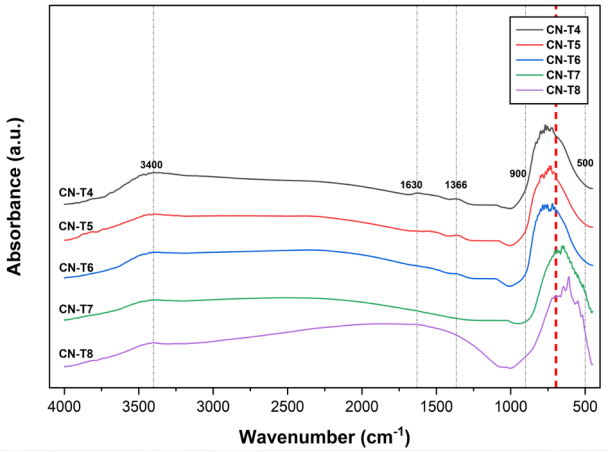


*Fig. 2. FTIR Spectra of Cu-Ni/$TiO_2$ nanoparticle.*

Fig. 3 shows the XRD patterns of Cu-Ni/$TiO_2$ nanoparticles annealed at a temperature of 400°C, 500°C, 600°C, 700°C, and 800°C. The main diffraction peak for anatase (JCPDS file no. 01-071-1166) at $2\theta = 25.66°$ while the main diffraction peak for rutile (JCPDS file no. 01-082-0514) at $2\theta = 27.82°$. For CN-T4 and CN-T5 samples, a diffraction peak at $2\theta$ value of 25.66° corresponds to the fully (101) anatase phase. For sample CN-T6, as the annealed temperature increases to 600°C, the mixed phase anatase-rutile formed with small peak intensity corresponding to (110) rutile phase at diffraction peak 27.82° and anatase phase as dominant peak. This mixed phase that formed indicates the beginning of anatase to rutile phase transformation [35]. Sample CN-T7 shows the dominant rutile phase after the annealing temperature of Cu-Ni/$TiO_2$ raised at 700°C. Thus, the total

transformation of anatase to rutile phase occurred after Cu-Ni/$TiO_2$ was annealed at 800°C for sample CN-T8.

The mole ratios of the structural phase for anatase and rutile phase were calculated based on the Spurr and Myers equation in Eq. (2) and (3) [36] due to the existence of two phases which are anatase and rutile phases that were established from the XRD diffraction peaks of the Cu-Ni/$TiO_2$ in Fig 3.,

$$W_R = \frac{1}{1+0.81\left(\frac{I_A}{I_R}\right)} \tag{2}$$

$$W_A = 1 - W_R \tag{3}$$

where $W_R$ and $I_R$ are the mole fraction and peak intensity of the rutile phase, respectively. Meanwhile, $W_A$ and $I_A$ are for the anatase phase. The intensity peaks at diffraction angles at 25.66° (101) and 27.82° (110) are taken as characteristic peaks for anatase and rutile phases, respectively. The percentage of anatase and rutile phase content was obtained by using Eq. (4) and (5) [37],

$$Anatase\ \% = \frac{100 \times I_A}{I_A + 1.265 \times I_R} \tag{4}$$

$$100 - A\ \% = Rutile\ \% \tag{5}$$

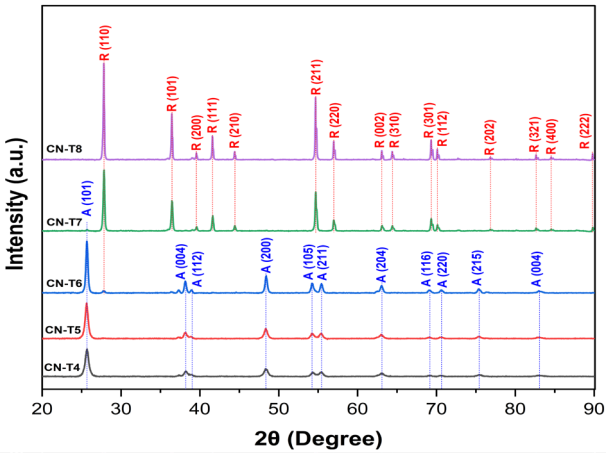


*Fig. 3. XRD patterns of Cu-Ni/$TiO_2$ annealed at different temperatures (A, anatase, and R, rutile).*

The effect of annealing temperature on the structural phase content of samples, as shown in Fig. 4, based on the mole fraction and phase content of anatase and rutile of Cu-Ni/$TiO_2$. As the annealing temperature rises, the anatase phase content decreases while the rutile phase content increases. The percentage of anatase phase for sample CN-T4 and CN-T5 are 100%, indicating the XRD pattern for the Cu-Ni/$TiO_2$ that annealed at below 500°C consists of anatase phase only. The transformation of the anatase to rutile phase occurred at an annealed temperature of 600°C in which the anatase phase consists of 95.19% while the rutile phase is 4.80%. Meanwhile, anatase's percentage of phase content decreased to 1.82%, while the rutile phase increased to 98.17% with the increment of annealing temperatures to 700°C. The transformation of anatase to a completely rutile phase occurred at an annealing temperature above 800°C with rutile phase content is 100%. Based on these results, we can conclude that both structural phases' mole fraction and phase content are reciprocal. The phase composition value for each sample summarized in Table 1.

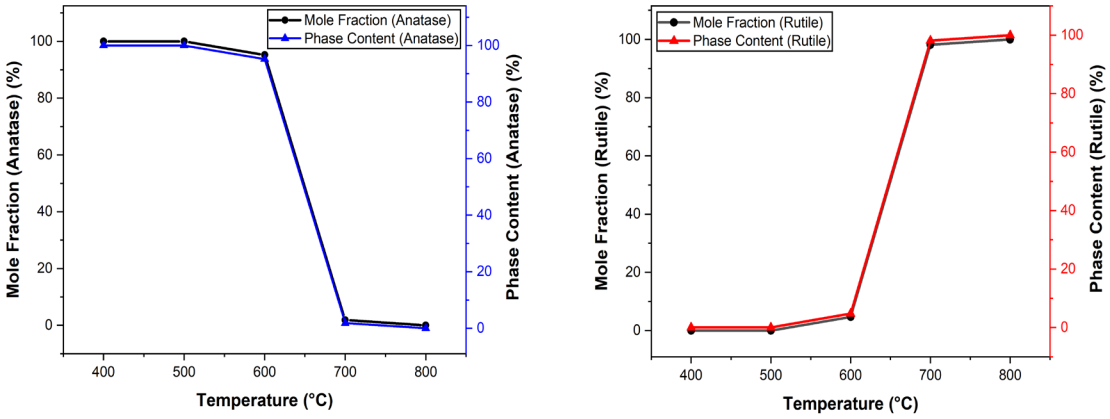


*(a)* *(b)*

*Fig. 4. Mole fraction and phase content of Cu-Ni/$TiO_2$ at different annealing temperature; (a) anatase phase; and (b) rutile phase.*

*Table 1. Mole fraction and phase composition values for each temperature.*

| Samples | Anatase | | Rutile | |
|---|---|---|---|---|
| | Mole fraction (%) | Phase content (%) | Mole fraction (%) | Phase content (%) |
| CN-T4 | 100 | 100 | 0 | 0 |
| CN-T5 | 100 | 100 | 0 | 0 |
| CN-T6 | 95.21 | 95.19 | 4.69 | 4.80 |
| CN-T7 | 1.83 | 1.82 | 98.12 | 98.17 |
| CN-T8 | 0 | 0 | 100 | 100 |

The estimated crystallite size of Cu-Ni/$TiO_2$ for each annealing temperature was estimated by using Debye-Scherrer in Eq. (6) [38].

$$D = \frac{0.9\lambda}{\beta\cos\theta} \tag{6}$$

where D is the crystallite size, β is the full width at half maximum (FWHM), λ is the X-ray wavelength (1.5406 Å), while θ is the diffraction angle. The estimated crystallite size for the sample CN-T4 to CN-T8 increased from 20.26 nm to 56.99 nm with the annealing temperature.

The specific surface area (SSA) is the total surface area of a solid material per unit of mass [39]. Based on the Eq. (7), the SSA of the samples can be calculated.

$$SSA = \frac{6\times10^3}{\rho D_P} \tag{7}$$

where ρ is the density of a nanoparticle and $D_P$ is the size of the nanoparticles [37]. Based on Fig. 5 (a) and (b), SSA in both structural phase anatase and rutile decrease after the annealing temperature increases, and it is inversely proportional to the crystallite size of photocatalyst. Table 2 shows the calculated data for the crystallite sizes and SSA for each annealing temperature's anatase and rutile phases. The photocatalytic activity of the photocatalyst is dependent on the crystallite size and surface area [13], [40], [41]. The small crystallite size increases the surface area of the photocatalyst, resulting in increases in the photocatalyst's adsorption efficiency to the reactant and absorption to the light source. [3], [8], [35].

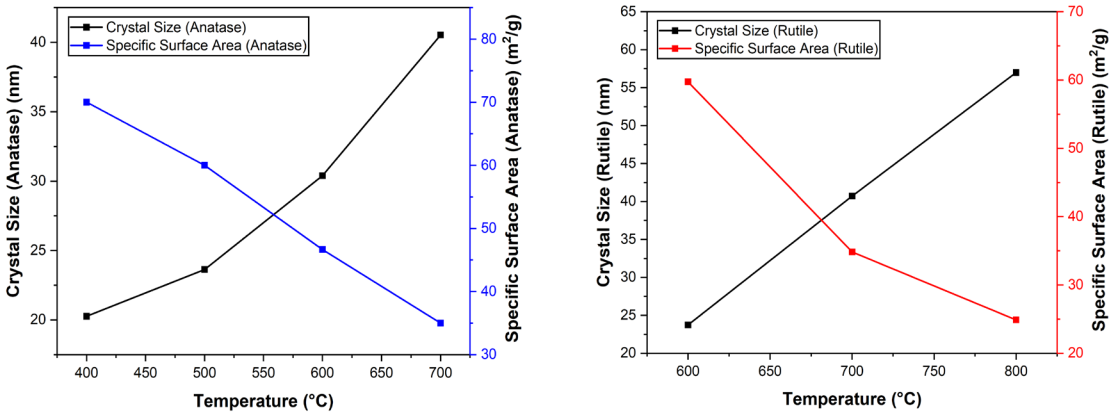


*(a)* *(b)*

*Fig. 5. Effect of annealing temperature on crystallite size and specific surface area (SSA) of Cu-Ni/$TiO_2$; (a) anatase phase;and (b) rutile phase.*

*Table 2. Crystal size and specific surface area for each annealing temperature.*

| Samples | Anatase | | Rutile | |
|---|---|---|---|---|
| | **Crystallite size (nm)** | **Specific surface area ($m^2/g$)** | **Crystallite size (nm)** | **Specific surface area ($m^2/g$)** |
| CN-T4 | 20.26 | 70.00 | - | - |
| CN-T5 | 23.64 | 60.01 | - | - |
| CN-T6 | 30.40 | 46.67 | 23.75 | 59.74 |
| CN-T7 | 40.53 | 35.00 | 40.71 | 34.84 |
| CN-T8 | - | - | 56.99 | 24.89 |

The estimated band gap of the annealed Cu-Ni/$TiO_2$ nanoparticles was calculated by using Kubelka-Munk function F(R) in Eq. (8)

$$F(R) = \frac{(1-R)^2}{2R} \tag{8}$$

where R is a reflectance percentage from diffuse reflectance spectra (DRS) for each sample. A graph of $(F(R)\ hv)^2$ vs $hv$ which $hv$ represents photon energy, was plotted to obtain the band gap of the Cu-Ni/$TiO_2$ nanoparticles. From Eq. (8), the extrapolation line of the Tauc plot to the $hv$ axis indicates the estimated band gap of each sample as shown in Fig. 6 (a)-(e). The estimated band gap values are tabled in Table 3.

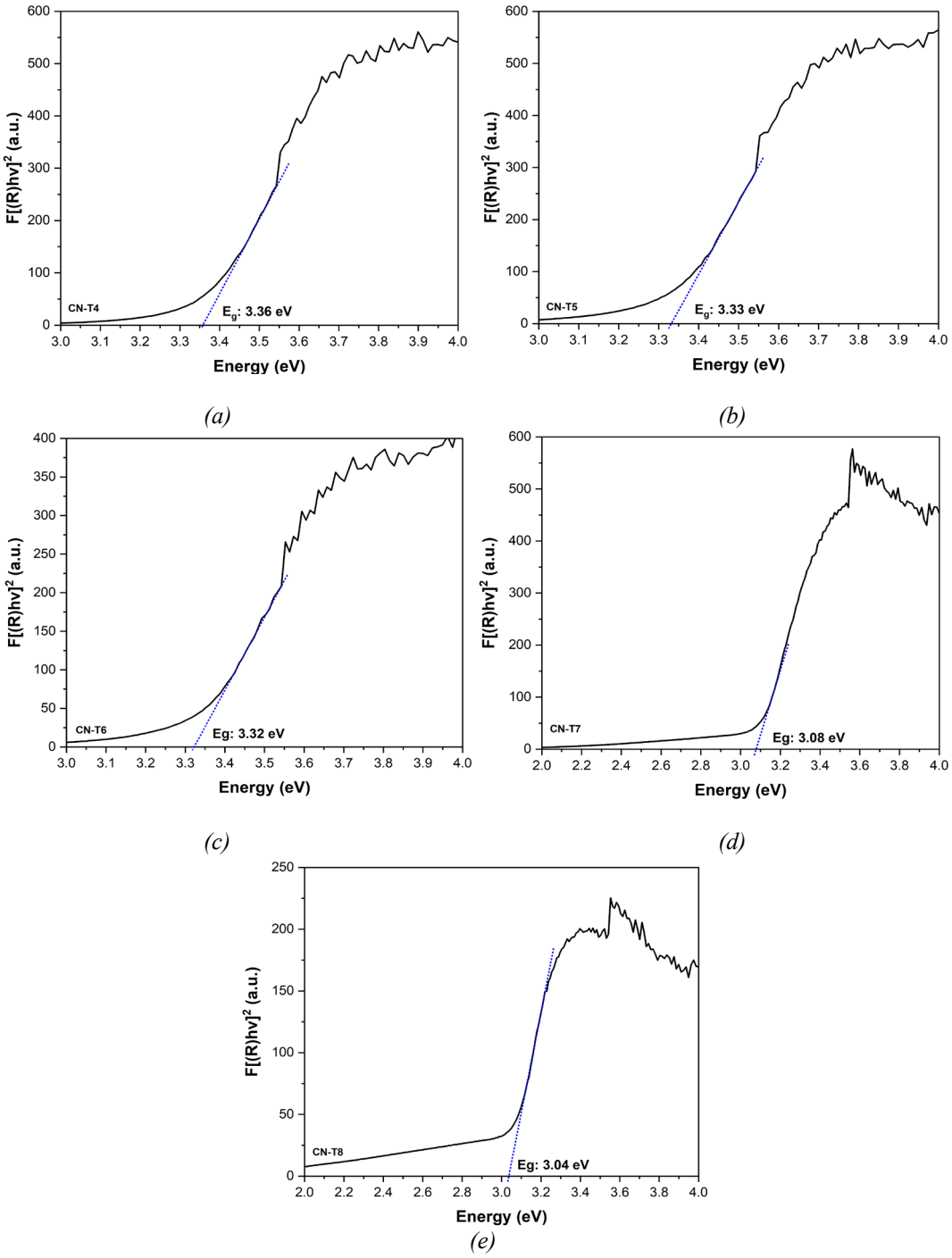


*Fig. 6. Estimation band gap (eV) of Cu-Ni/$TiO_2$ annealed at different temperatures; (a) CN-T4; (b) CN-T5; (c) CN-T6; (d) CN-T7; and (e) CN-T8.*

*Table 3. Estimation band gap of Cu-Ni/$TiO_2$ at different anneal temperature.*

| Samples | Annealing temperature (°C) | Band gap (eV) |
|---|---|---|
| CN-T4 | 400 | 3.36 |
| CN-T5 | 500 | 3.33 |
| CN-T6 | 600 | 3.32 |
| CN-T7 | 700 | 3.08 |
| CN-T8 | 800 | 3.04 |

The crystallite size increase with the annealing temperature rises, resulting in a decrease in the estimated band gap. The crystallite sizes of the photocatalyst can explain these results are the factor that can affect the band gap values of the Cu-Ni/$TiO_2$ [3], [8], [35]. As the annealing temperature rises, the interatomic spacing of the crystallite structure is reduced, and it changes the photocatalyst's structural phase [8]. A relation between annealing temperature, crystallite size, and band gap was identified by Eq. 9,

$$Annealing\ temperature \propto \frac{Crystal\ size}{Bandgap\ energy} \tag{9}$$

where annealing temperature is directly proportional to crystallite size and inversely proportional to band gap [35], [37]. These results also correspond to the previous study in which the changes of band gap are dependent on the size of crystallite [3], [9], [18].

According to the H. Lin et al., as a particle size decrease, the density of point/surface defects of semiconductors increases. These defects will create deep and shallow traps near the semiconductor's conduction band. This situation will cause the delocalization of molecular orbitals in the semiconductor surface [42]. Deep traps are localized in space at lattice site defects, which lie in the middle of the band gap. Meanwhile, the shallow traps lie within a few meV near the conduction band (lowest unoccupied molecular orbital, LUMO) [43]. When the size of a semiconductor particle decreases below its bulk of Bohr radius ($r_{Bohr}$) at the first excitation state, the size of quantization (Q-size) of the particle rises due to the spatial confinement of the charge carrier. Thus, the shallow traps will shift to higher energy, resulting in blue shifting of the absorption spectra. This phenomenon has been described by Brus' effective-mass model (EMM) [42].

The surface morphology of the annealed Cu-Ni/$TiO_2$ at different annealing temperatures are depicted in Fig. 7 (a)-(e). Based on the FESEM image shows an irregular-sized spherical with an agglomeration of a particle on the morphology of the Cu-Ni/$TiO_2$. The agglomerations might occur due to overlapping small and medium size particles [8]. Riaz N. et al. [2] and Bashiri R. et al. [44] also reported the agglomeration for Cu-Ni/$TiO_2$ due to the high annealing temperature. As the annealing temperature increases, the degree of agglomeration of the Cu-Ni/$TiO_2$ increases due to the crystallite size growth. These results are also related to the changes in the particle's structural phase with the transformation of anatase to rutile with annealed temperature raises, as shown in XRD results [33], [45]. Table 3 shows the average particle size for all the samples. These FESEM results agree with XRD analysis that the crystallite size increased when the annealing temperature raised.

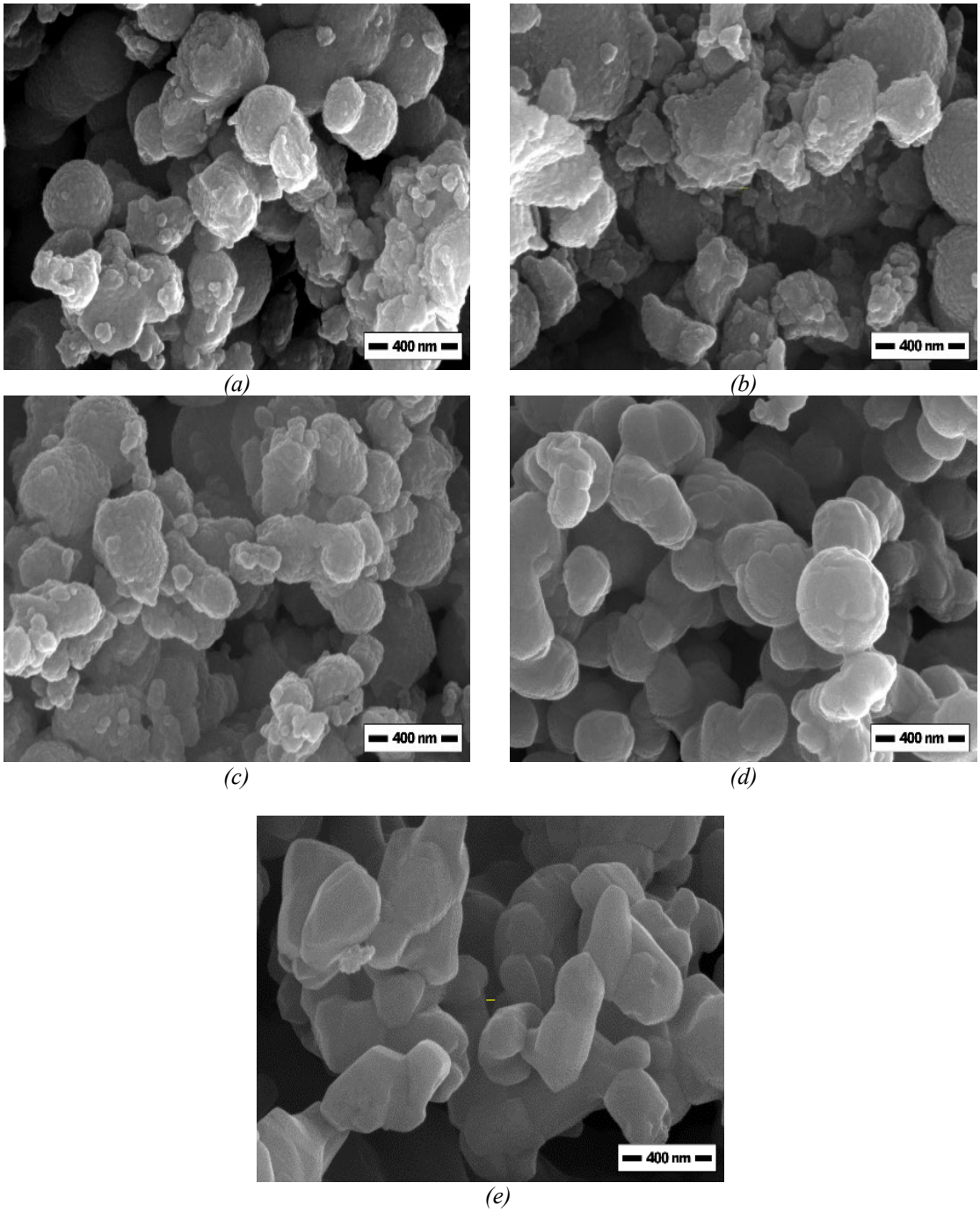


*Fig. 7. FESEM images of Cu-Ni/$TiO_2$ annealed at different temperatures; (a) CN-T4; (b) CN-T5; (c) CN-T6; (d) CN-T7; and (e) CN-T8.*

*Table 3. The size range of the particle of the annealed Cu-Ni/$TiO_2$.*

| Samples | Annealing temperature (°C) | Average Particle Size (nm) |
|---|---|---|
| CN-T4 | 400 | 38.52 |
| CN-T5 | 500 | 49.81 |
| CN-T6 | 600 | 59.49 |
| CN-T7 | 700 | 89.33 |
| CN-T8 | 800 | 173.59 |

Fig. 8 depicts the EDX spectrum elemental for EDX mapping and plotting of Cu-Ni/$TiO_2$ annealed at 400° C. Based on the EDX spectrum elemental in Fig. 8 (a), revealed the elemental composition of O, Ti, Cu, Ni and Au elements as shown in Table 4. Gold element peak was detected in the EDX system because of the gold sputtering used in sample preparation for FESEM/EDX measurement to reduce the charging effect and generate a clearer image of the sample [46]. Fig. 8 (b-f) indicates the EDX colour mapping of the individual Ti, O, Cu, Ni and Au elements from the selected area, which, based on the colour mapping, the presence of Cu-Ni on the surface of $TiO_2$ is confirmed.

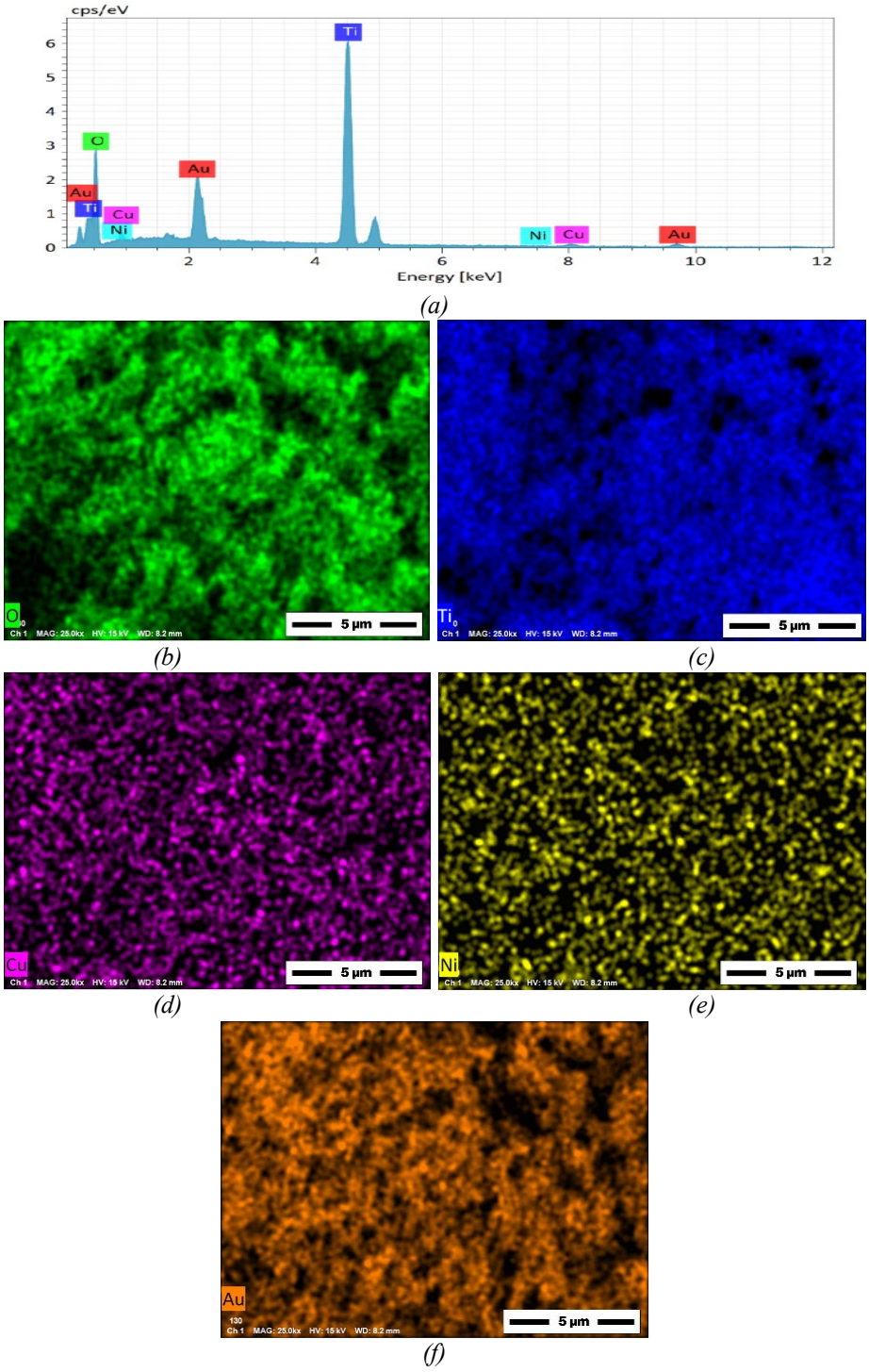


*Fig. 8. EDX mapping and plotting of Cu-Ni/$TiO_2$ annealed at 400 °C; (a) EDX spectra; (b) oxygen; (c) titanium; (d) copper; (e) nickel; and (f) gold.*

*Table 4. Spectrum point of EDX spectrum for Cu-Ni/$TiO_2$.*

| Elements | Mass (wt%) |
|---|---|
| Oxygen | 28.38 |
| Titanium | 53.70 |
| Nickel | 0.11 |
| Copper | 2.66 |
| Gold | 12.99 |

The photocatalytic performance of the annealed Cu-Ni/$TiO_2$ was evaluated in the degradation of methylene blue (MB) under UV light irradiation. Fig. 9 (a)-(e) presents the changes in MB absorption spectra of MB dye at different times for each sample.

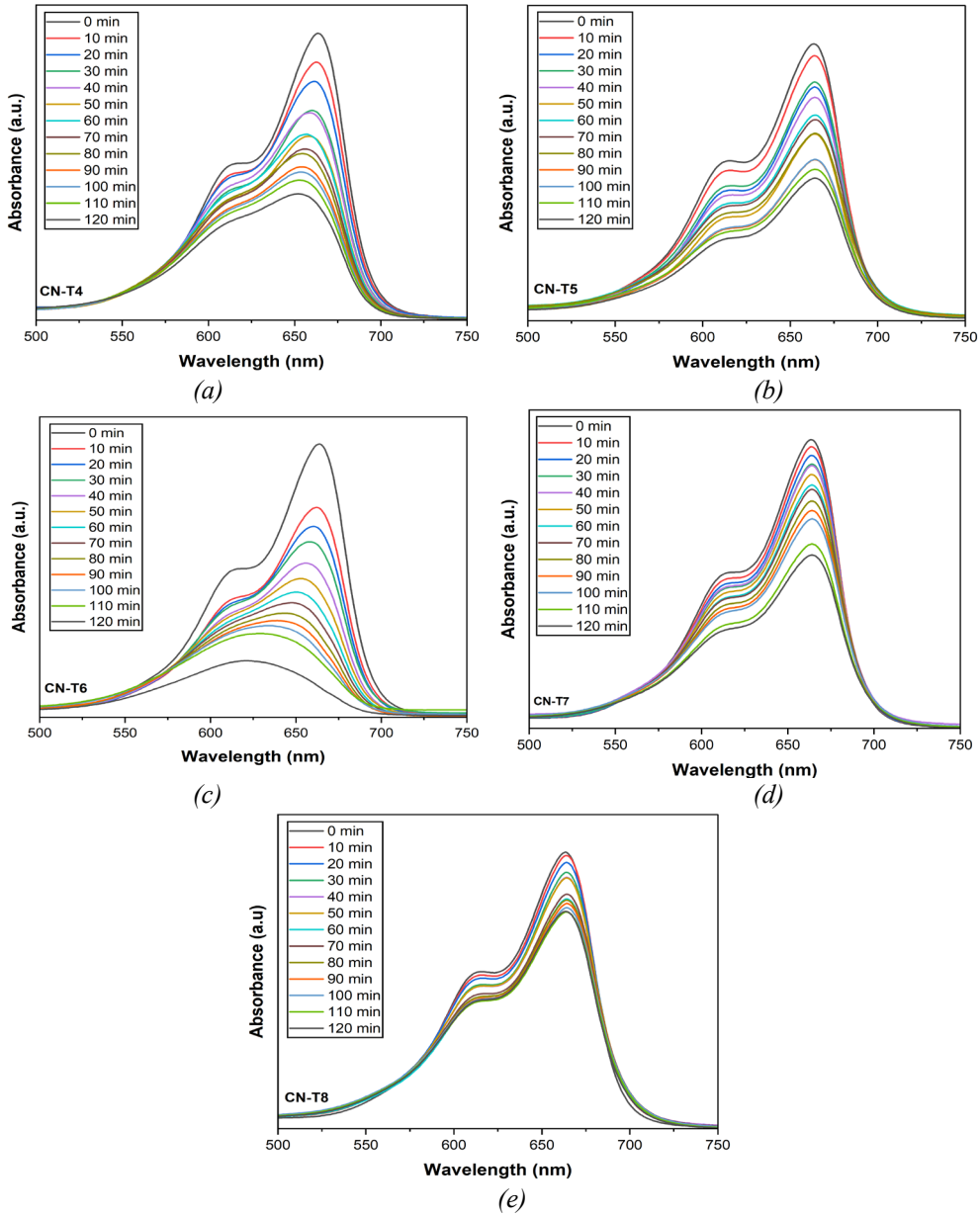


*Fig. 9. Absorption spectra changes of methylene blue under UV light irradiation for different time periods; (a) CN-T4; (b) CN-T5; (c) CN-T6; (d) CN-T7; and (e) CN-T8.*

The highest peak at 664 nm reduces gradually with the elapsed UV light irradiation period, resulting the CN-T6 exhibiting the highest photocatalytic efficiency, which CN-T6 shows the lowest absorption spectra after 120 mins UV light irradiation compared to other samples.

This result is also in valid agreement with photocatalytic efficiency and degradation percentage (%) in the degradation of 10 ppm MB depicted in Fig. 10 (a) and (b), with CN-T6 exhibiting the highest degradation percentage, 62.81% of MB after 120 min UV light irradiation.

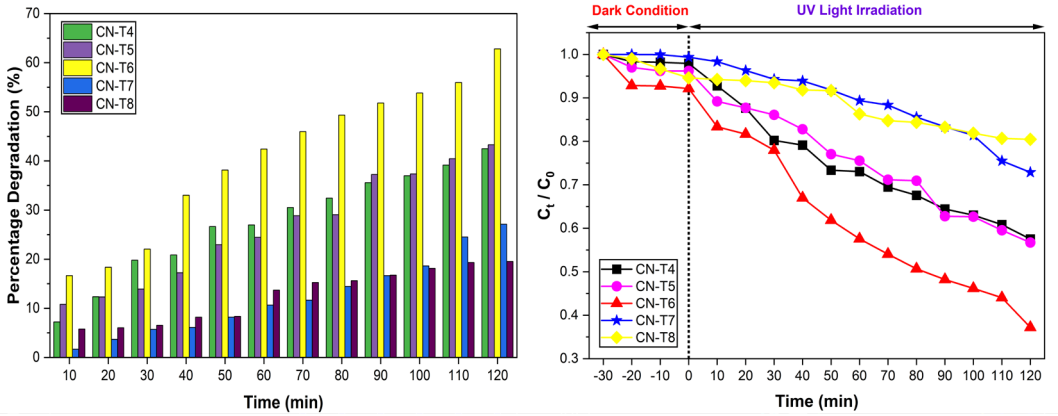


*Fig. 10. Photocatalytic performance of the degradation 10 ppm MB under UV light irradiation; (a) Photocatalytic degradation curve; and (b) Photodegradation percentage.*

The first-order rate constant depicted in Fig. 11 is calculated by using Eq. (10) [18]

$$ln\left(\frac{C_0 - C_t}{C_0}\right) = kt \tag{10}$$

where $\boldsymbol{C_0}$ is the initial concentration, $\boldsymbol{C_t}$ is the concentration of the MB after photocatalytic reaction for time, $\boldsymbol{t}$ and $\boldsymbol{k}$ is the first-order constant. Table 5 shows the degradation percentage and degradation rate constant, in which the order of MB degradation from the highest to the lowest value for photocatalytic efficiency is CN-T6 > CN-T5 > CN-T4 > CN-T7 > CN-T8. These results also can be observed clearly in the images of photodegradation of Cu-Ni/$TiO_2$ displayed in Fig.12 (a) and (b). CN-T6 closest to completely decomposing MB and CN-T4 and CN-T5 partially decompose. Meanwhile, CN-T7 and CN-T8, consisting of rutile dominant and single rutile phases, hardly degrade MB after 120 min UV light irradiation. Thus, these results are consistent with the study of B. Anitha et al., in which the photocatalytic performance is reduced with the increment of rutile phase content [35]. These results are due to the anatase phase having an indirect band gap and the rutile having a direct band gap. The indirect band gap exhibits longer electron-hole pair recombination lifetimes, which lower the rate of recombination of electron-hole pairs. While the rutile phase has a fast recombination rate leading to low photocatalytic performance [18]. The anatase-rutile mixed phase exhibits the most excellent photocatalytic performance due to the synergistic effect, which indicates that the photoexcitation charge carriers of the anatase phase more easily migrate and transfer to the surface of the rutile phase. These results provide more efficient electron-hole separation by reducing the recombination of photogenerated electrons and holes [47].

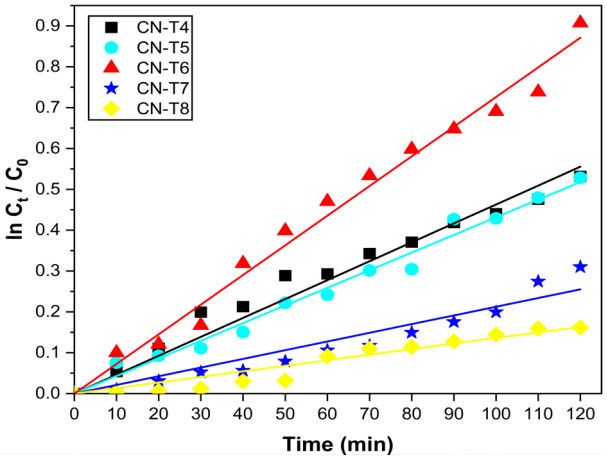


*Fig. 11. Photocatalytic degradation rate constant of methylene blue for annealed Cu-Ni/$TiO_2$ at different temperatures.*

*Table 5. Photocatalytic degradation percentage and rate constant.*

| Sample | Photocatalytic Degradation (%) | Photocatalytic Rate Constant ($min^{-1}$) |
|---|---|---|
| CN-T4 | 42.48 | $4.63\times10^{-2}$ |
| CN-T5 | 43.29 | $4.32\times10^{-2}$ |
| CN-T6 | 62.81 | $7.26\times10^{-2}$ |
| CN-T7 | 27.13 | $2.13\times10^{-2}$ |
| CN-T8 | 19.53 | $1.36\times10^{-2}$ |

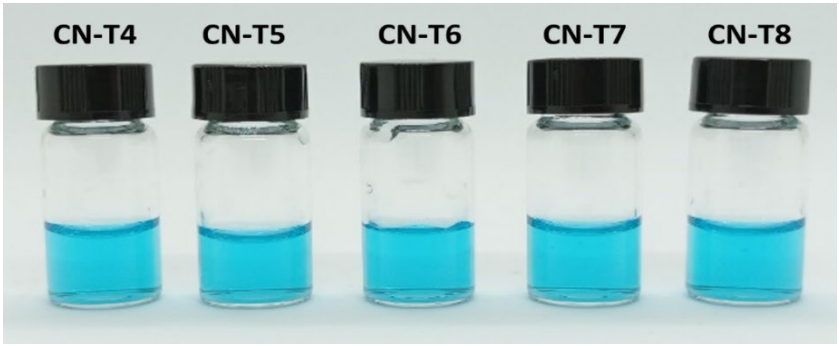


*(a)*

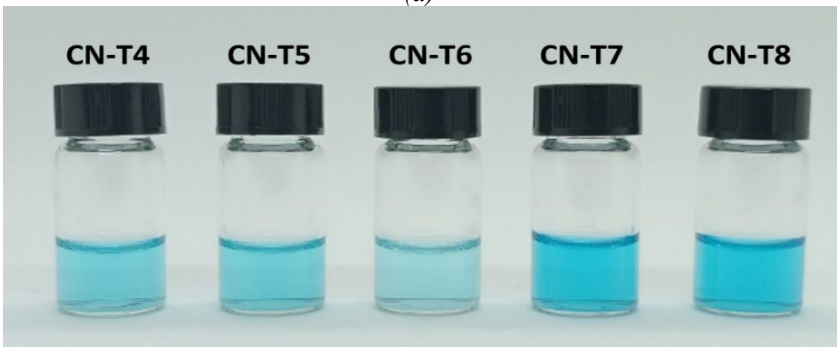


*(b)*

*Fig. 12. Images of methylene blue photodegradation by Cu-Ni/$TiO_2$ (a) initial (t = 0 min); and (b) final (t = 120 min).*

The photocatalytic performance of photocatalysts depends on many factors, including structural phase composition, crystallite size, surface area and band gap [3], [8], [48]. Based on all these photocatalytic results, CN-T6 is the highest photocatalytic efficiency for this study. It shows that the mixed anatase/rutile phase with anatase as a dominant phase resulting higher photoactivity performance compared to the single anatase or rutile phase contents. Based on the XRD result, the annealing temperature affected the crystallite size of the photocatalyst, resulting in a smaller size at a low annealing temperature. Small crystallite size exhibits the high specific surface area of the photocatalyst [35]. Photocatalysts with large surface areas can adsorb many organic compounds at active sites on the photocatalyst surface by forming $Ti^{4+}$ $^{-}OH_2$ on the active site photocatalyst's surface [49]–[51]. The increase of the surface adsorption site causes a reduction in the dye degradation period [8]. According to L. Gonghu et al., although the specific surface area of pure anatase is larger than the mixed phase of $TiO_2$, most of the previous studies [2], [8], [13] reported that the anatase rutile mixed phase with anatase as the dominant phase content has higher photocatalytic efficiency compared to the pure anatase phase [49]. This is because the presence of tetrahedral $Ti^{4+}$ sites in the mixed phase, as suggested by Depero [52] contributes to enhancing the photocatalytic efficiency of the photocatalyst [49].

## 4. Conclusions

In this study, Cu-Ni/$TiO_2$ nanoparticles was annealed at different temperatures ranging from 400 to 800°C to study the effect of annealing temperature on its structural, morphological, and optical properties. The annealing temperature affected the crystallite size, phase transformation, structural phase, surface area, band gap, and degree of agglomeration of the particles based on XRD, FESEM, UV-DRS and Visible Spectrophotometer analysis. The XRD patterns have shown that Cu-Ni/$TiO_2$ was composed of a single anatase phase at 400 and 500°C, mixed phase anatase-rutile phases at 600 and 700°C, and a single rutile phase at 800°C. As the annealing temperature raised, the crystallite size of the Cu-Ni/$TiO_2$ increased from 20.26 to 56.99 nm, and the specific surface area of the samples decreased from 70.00 to 24.89 $m^2/g$.

The band gap of the annealed Cu-Ni/$TiO_2$ reduced from 3.36 to 3.04 eV with the increment of annealing temperature. FESEM shows the degree of agglomeration of the Cu-Ni/$TiO_2$ increases with the annealing temperature due to the crystallite size growth. EDX results revealed that the copper and nickel were successfully doped in the photocatalyst. In this study, the anatase-rutile mixed phase with anatase as a dominant phase (CN-T6) demonstrated the highest photocatalytic performance with 62.81% of the degradation percentage and $7.26\times10^{-2}$ $min^{-1}$ for the photocatalytic rate constant of MB removal. In conclusion, annealing temperature affects photocatalytic efficiency by changing the phase composition and crystallinity of the photocatalyst.

**Acknowledgements**

This research was supported with Kurita Overseas Research Grant (22Pmy215-U2) provided by Kurita Water and Environment Foundation. The authors would like to thank the Faculty of Applied Sciences, UiTM Shah Alam, Selangor, for their sample characterization facilities.

## References

[1] S. Phromma, T. Wutikhun, P. Kasamechonchung, T. Eksangsri, and C. Sapcharoenkun, Appl. Sci., 10, 3, (2020); https://doi.org/10.3390/app10030993
[2] N. Riaz, F. K. Chong, B. K. Dutta, Z. B. Man, M. S. Khan, and E. Nurlaela, Chem. Eng. J., 185–186, 108–119, (2012); https://doi.org/10.1016/j.cej.2012.01.052
[3] M. Lal, P. Sharma, and C. Ram, Optik (Stuttg)., 241(March), 166934, (2021); https://doi.org/10.1016/j.ijleo.2021.166934

[4] A. C. Lee, R. H. Lin, C. Y. Yang, M. H. Lin, and W. Y. Wang, Mater. Chem. Phys., 109(2–3), 275–280, (2008); https://doi.org/10.1016/j.matchemphys.2007.11.016
[5] J. Nisar, Z. Topalian, A. De Sarkar, L. Österlund, and R. Ahuja, ACS Appl. Mater. Interfaces, 5(17), 8516–8522, (2013); https://doi.org/10.1021/am4018835
[6] J. Sun, Y. X. Wang, M. Xu, T. L. Ma, and X. Y. Fan, Mater. Sci. Forum, 663–665, 848–851, (2011); https://doi.org/10.4028/www.scientific.net/MSF.663-665.848
[7] L. Yang, A. Cai, C. Luo, Z. Liu, W. Shangguan, and T. Xi, Sep. Purif. Technol., 68(2), 232–237, (2009); https://doi.org/10.1016/j.seppur.2009.05.008
[8] D. K. Muthee and B. F. Dejene, Heliyon, 7(6), (2021); https://doi.org/10.1016/j.heliyon.2021.e07269
[9] M. K. Singh and M. S. Mehata, Optic, 193(April), 163011, (2019); https://doi.org/10.1016/j.ijleo.2019.163011
[10] R. S. Dubey, Mater. Lett., 215, 312–317, (2018); https://doi.org/10.1016/j.matlet.2017.12.120
[11] M. R. Al-Mamun, S. Kader, M. S. Islam, and M. Z. H. Khan, J. Environ. Chem. Eng., 7(5), (2019); https://doi.org/10.1016/j.jece.2019.103248
[12] D. A. H. Hanaor and C. C. Sorrell, J. Mater. Sci., 46(4), 855–874, (2011); https://doi.org/10.1007/s10853-010-5113-0
[13] N. Yuangpho, S. T. T. Le, T. Treerujiraphapong, W. Khanitchaidecha, and A. Nakaruk, Phys. E Low-Dimensional Syst. Nanostructures, 67, 18–22, (2015); https://doi.org/10.1016/j.physe.2014.11.006
[14] Q. Zhang, L. Gao, and J. Guo, Appl. Catal. B Environ., 26(3), 207–215, (2000); https://doi.org/10.1016/S0926-3373(00)00122-3
[15] Z. Zhang, C. C. Wang, R. Zakaria, and J. Y. Ying, J. Phys. Chem. B, 102(52), 10871–10878, (1998); https://doi.org/10.1021/jp982948+
[16] J. He et al., Molecules, 24(2996), 1–14, (2019); https://doi.org/10.3390/molecules24162996
[17] W. Fu et al., Chem. Commun., 54(1), 58–61, (2017); https://doi.org/10.1039/c7cc05750d
[18] M. G. Kim et al., ACS Omega, 6(16), 10668–10678, (2021); https://doi.org/10.1021/acsomega.1c00043
[19] M. Wang, Q. Zhao, H. Yang, D. Shi, and J. Qian, Ceram. Int., 46(10), 16716–16724, (2020); https://doi.org/10.1016/j.ceramint.2020.03.246
[20] Y. Liu, Z. Wang, W. Fan, Z. Geng, and L. Feng, Ceram. Int., 40(3), 3887–3893, (2014); https://doi.org/10.1016/j.ceramint.2013.08.030
[21] R. D. Desiati, M. Taspika, and E. Sugiarti, Mater. Res. Express, 6(9), (2019); https://doi.org/10.1088/2053-1591/ab155c
[22] M. Crişan et al., 504, 130–142, (2015); https://doi.org/10.1016/j.apcata.2014.10.031
[23] L. S. Yoong, F. K. Chong, and B. K. Dutta, 34(10), 1652–1661, (2009); https://doi.org/10.1016/j.energy.2009.07.024
[24] D. Jing, Y. Zhang, and L. Guo, Chem. Phys. Lett., 415(1–3), 74–78, (2005); https://doi.org/10.1016/j.cplett.2005.08.080
[25] H. Dong et al., Water Research, 79, 128–146, (2015); https://doi.org/10.1016/j.watres.2015.04.038
[26] M. R. D. Khaki, M. S. Shafeeyan, A. A. A. Raman, and W. M. A. W. Daud, J. Environ. Manage., 198, 78–94, (2017); https://doi.org/10.1016/j.jenvman.2017.04.099
[27] M. A. Behnajady and H. Eskandarloo, J. Nanosci. Nanotechnol., 13(1), 548–553, (2013); https://doi.org/10.1166/jnn.2013.6859
[28] M. Shaban, A. M. Ahmed, N. Shehata, M. A. Betiha, and A. M. Rabie, J. Colloid Interface Sci., 555, 31–41, (2019); https://doi.org/10.1016/j.jcis.2019.07.070
[29] M. Gurulakshmi, M. Selvaraj, A. Selvamani, P. Vijayan, N. R. S. Rekha, and K. Shanthi, Appl. Catal. A, Gen., 449, 31–46, (2012); https://doi.org/10.1016/j.apcata.2012.09.039
[30] Z. Luo et al., Chem. Mater., 27(1), 6–17, (2015), https://doi.org/10.1021/cm5035112
[31] P. Kundu, A. Kaur, S. K. Mehta, and S. K. Kansal, J. Nanosci. Nanotechnol., 14(9), 6991–6995, (2014); https://doi.org/10.1166/jnn.2014.9238
[32] X. Yan, J. He, D. G. Evans, Y. Zhu, and X. Duan, J. Porous Mater., 11(3), 131–139, (2004); https://doi.org/10.1023/B:JOPO.0000038008.86521.9a

[33] S. Sugapriya, R. Sriram, and S. Lakshmi, Optik (Stuttg)., 124(21), 4971–4975, (2013); https://doi.org/10.1016/j.ijleo.2013.03.040
[34] J. L. Li and T. Inui, Appl. Catal. A Gen., 137(1), 105–117, (1996); https://doi.org/10.1016/0926-860X(95)00284-7
[35] B. Anitha and M. A. Khadar, Solid State Sci., 108(February), 106392, 2020; https://doi.org/10.1016/j.solidstatesciences.2020.106392
[36] D. K. Muthee and B. F. Dejene, Mater. Sci. Semicond. Process., 106(October), 104783, (2020); https://doi.org/10.1016/j.mssp.2019.104783
[37] M. Khalid Hossain et al., Mater. Sci. Pol., 35(4), 868–877, (2017); https://doi.org/10.1515/msp-2017-0082
[38] F. B. Dejene et al., Cent. Eur. J. Phys., 9(5), 1321–1326, (2011), https://doi.org/10.2478/s11534-011-0050-3
[39] B. Akbari, M. P. Tavandashti, and M. Zandrahimi, Iran. J. Mater. Sci. Eng., 8(2), 48–56, 2011.
[40] S. Ibrahim et al., Inorg. Chem. Front., 5(8), 1816–1827, (2018); https://doi.org/10.1039/c8qi00355f
[41] S. Notodarmojo, D. Sugiyana, M. Handajani, E. Kardena, and A. Larasati, J. Eng. Technol. Sci., 49(3), 340–357, (2017), https://doi.org/10.5614/j.eng.technol.sci.2017.49.3.4
[42] H. Lin, C. P. Huang, W. Li, C. Ni, S. I. Shah, and Y. H. Tseng, Appl. Catal. B Environ., 68(1–2), 1–11, (2006); https://doi.org/10.1016/j.apcatb.2006.07.018
[43] L. Brus, J. Phys. Chem., 90(12), 2555–2560, (1986), https://doi.org/10.1021/j100403a003
[44] R. Bashiri, N. M. Mohamed, F. K. Chong, and S. Sufian, Adv. Mater. Res., 925, 396–400, (2014), https://doi.org/10.4028/www.scientific.net/AMR.925.396
[45] D. J. Kim, S. H. Hahn, S. H. Oh, and E. J. Kim, Mater. Lett., 57(2), 355–360, (2002); https://doi.org/10.1016/S0167-577X(02)00790-5
[46] H. Hamidinezhad, A. A. Ashkarran, and Z. Abdul-Malek, Silicon, 9(3), 379–384, (2017); https://doi.org/10.1007/s12633-016-9424-x
[47] S. Bagheri and N. M. Julkapli, Rev. Inorg. Chem., 37(1), 11–28, (2017); https://doi.org/10.1515/revic-2016-0001
[48] N. Riaz, M. A. Bustam, F. K. Chong, Z. B. Man, M. S. Khan, and A. M. Shariff, Sci. World J., 2014, (2014); https://doi.org/10.1155/2014/342020
[49] G. Li, N. M. Dimitrijevic, L. Chen, J. M. Nichols, T. Rajh, and K. A. Gray, J. Am. Chem. Soc., 130(16), 5402–5403, (2008), https://doi.org/10.1021/ja711118u
[50] E. M. Seftel, M. Mertens, and P. Cool, Appl. Catal. B Environ., 134–135, 274–285, (2013); https://doi.org/10.1016/j.apcatb.2013.01.032
[51] B. Choudhury and A. Choudhury, Int. Nano Lett., 3(1), 1–9, (2013); https://doi.org/10.1186/2228-5326-3-55
[52] L. E. Depero, Journal of Solid State Chemistry, 104(2). 470–475, (1993); https://doi.org/10.1006/jssc.1993.1184